Research Square

Preprints are preliminary reports that have not undergone peer review.
They should not be considered conclusive, used to inform clinical practice,
or referenced by the media as validated information.

Acridinone-Sulfonamide Hybrids: Synthesis, photophysical properties, DFT Analysis, and Antiviral Docking Against Adenovirus

Shanmugavel Balamurugan
Vellore Institute of Technology University
Vijayaparthasarathi Vijayakumar
vvijayakumar@vit.ac.in

Vellore Institute of Technology University

Article

Keywords:

Posted Date: February 5th, 2026

DOI: https://doi.org/10.21203/rs.3.rs-8612328/v1

License: This work is licensed under a Creative Commons Attribution 4.0 International License.
Read Full License

Additional Declarations: No competing interests reported.

Version of Record: A version of this preprint was published at Scientific Reports on September 15th, 2026. See the published version at https://doi.org/10.1038/s41598-026-65282-1.

Acridinone-Sulfonamide Hybrids: Synthesis, photophysical properties, DFT Analysis, and Antiviral Docking Against Adenovirus

Shanmugavel Balamurugan, Vijayaparthasarathi Vijayakumar*.

Department of Chemistry, School of Advanced Sciences, Vellore Institute of Technology, Vellore-632014, Tamilnadu, India.

*Corresponding Author: Vijayaparthasarathi Vijayakumar

Corresponding author email id*: vvijayakumar@vit.ac.in; kvpsvijayakumar@gmail.com*

Abstract

In this investigation, acridinone-based sulfonamides **6a-6j** and **10a-10j** were synthesized, and their structures were characterized using various spectroscopic techniques. Density Functional Theory (**DFT)** calculations indicated that the introduction of electron-withdrawing group(s) stabilizes the molecular orbital energy gap between **HOMO-LUMO**. Adding an electron-withdrawing group in the para position enhances both the reactivity and molecular softness of the compounds. Molecular electrostatic potential (MEP) mapping revealed that the carbonyl and sulfonyl functional groups serve as primary nucleophilic sites, facilitating interactions with various active biological receptors. Molecular docking studies against the target protein (PDB ID: 9cm2) indicated that compounds **6d**, **6h**, and **10d** possess the highest binding affinities, ranging from -11.1 to -10.8 kcal/mol, and exhibit the lowest inhibition constants (**Ki**). These compounds were compared with the standard antiviral drug cidofovir, which demonstrates multiple hydrogen bonding, π-π stacking, π-sulfur interactions, and hydrophobic interactions that enhance binding activity. Photophysical studies revealed that the **10a-10j** compounds exhibit improved emission properties with high quantum yields. Overall, the **10a-10j** compounds exhibit effective fluorescence, and specific compounds have been identified as potential antiviral leads for further investigation.

1. Introduction

Quinoline is present in small amounts in plants as quinoline alkaloids and is also found in coal tar. It has been commonly synthesized in laboratories and industries using the Skraup [1], Friedlander [2], Doebner-Miller [3], and Combes [4] methods, in which condensation, cyclization, and oxidation lead to aromatization. Quinoline and its derivatives play a vital role in pharmaceuticals, due to their core structure and various heteroatom modifications. The primary

reason for quinoline's medicinal activity lies in its aromatic ring system, which includes a nitrogen atom. This structure allows for metal chelation [5] and facilitates structural modifications. Even small changes to the core structure can result in significant activity against a range of conditions, including malaria [6], bacterial infections [7], cancer [8], inflammation [9], diabetes [10], and viral infections [11]. Additionally, Quinoline and its derivatives exhibit strong fluorescence, attributed to their extensive π-conjugated aromatic structures and the presence of a heteroaromatic nitrogen atom. The combination of benzene and pyridine rings enables quinoline to undergo π-π* and n-π* electronic transitions when exposed to UV-Visible light. The nitrogen atom in the core is crucial for intramolecular charge transfer (ICT), which enhances its luminescent properties. One notable derivative, 8-hydroxyquinoline, is known for forming highly fluorescent metal chelates, such as *tris*(8-hydroxyquinolinato) aluminium (AlQ_3), which are utilised in organic light-emitting diodes (OLEDs) and photonic devices [12–15]**.** Quinoline compounds are also used in synthetic dyes and exhibit photochemical properties due to the extended delocalization of π-electrons in the aromatic ring, their solubility, and the ability of the nitrogen atom to coordinate with metals. Variations in substitutions on the quinoline ring contribute to fluorescence, yielding bright, long-lasting colors [16]. Moreover, quinoline is widely employed in fluorescence and colorimetric sensors due to its unique photophysical and electronic properties. The nitrogen atom in quinoline effectively binds to metal ions in food materials, forming stable metal complexes with Cu^{2+}, Fe^{3+}, Pb^{2+}, and Cd^{2+}, which can alter the absorption and emission spectra [17–19].

The sulfonamide functional group (-SO_2NH-) attached to the quinoline ring has increasingly been recognized as an important pharmacophore in drug development [20–22]. Sulfonamides are notable for their strong hydrogen-bonding capability, adjustable acidity and basicity, and remarkable conformational stability, which allows them to serve as bioisosteres for ureas [23], carbamates [24], and other sulfonamides. Due to their balanced hydrophilicity and lipophilicity, sulfonamides often enhance drug solubility, permeability, and metabolic stability. Numerous FDA-approved drugs, including sulfonamide antibiotics [25], HIV protease inhibitors [26], and carbonic anhydrase inhibitors [27], highlight the clinical significance of sulfonyl-based functional groups. Small modifications to sulfonamide compounds can improve interactions with enzyme active sites, receptor binding pockets, and metal ions, thereby enhancing their pharmacokinetic and pharmacodynamic profiles.

Sulfonamide-substituted quinoline derivatives utilise the electron density in the quinoline ring, along with the strong H-bonding and polarity features of the sulfonamide group [28]. This

improves molecular recognition, binding to biological targets, and enhances the overall physicochemical properties of the compounds [29]. Also, sulfonamide derivatives are effective across various medicinal fields, including antimicrobial, anticancer, antiviral, anti-inflammatory, and enzyme-inhibitory applications [30].

In antimicrobial studies, sulfonamide-functionalized quinoline derivatives have demonstrated potent activity against Gram-positive and Gram-negative bacteria [31], fungi [32], and drug-resistant strains [33]. The disruption of membrane function, combined with the sulfonamide group's interaction with enzymes, results in broad-spectrum antimicrobial effects. These hybrids show promising activity in antimalarial detoxification pathways and interfere with parasite-specific redox processes [34,35]. In cancer treatment, sulphonamide-based quinoline derivatives exhibit cytotoxicity through mechanisms such as targeting topoisomerase in cancer cells and enhancing the water solubility, which is crucial for systemic delivery [36–38].

Sulfonamide derivatives act as enzyme inhibitors [39], particularly targeting metalloproteinases [40] and dihydrofolate reductase. Structural modification in sulfonamide derivatives acts as a zinc-binding group, allowing strong coordination with the active site of the metal ions [41]. The quinoline ring participates in hydrophobic and π-π stacking interactions. This ability to target multiple enzymes has made sulfonamide quinoline derivatives more effective as anti-inflammatory agents [42], anti-diabetic agents [43], anti-tuberculosis agents [44], and neuroprotective agents [45,46].

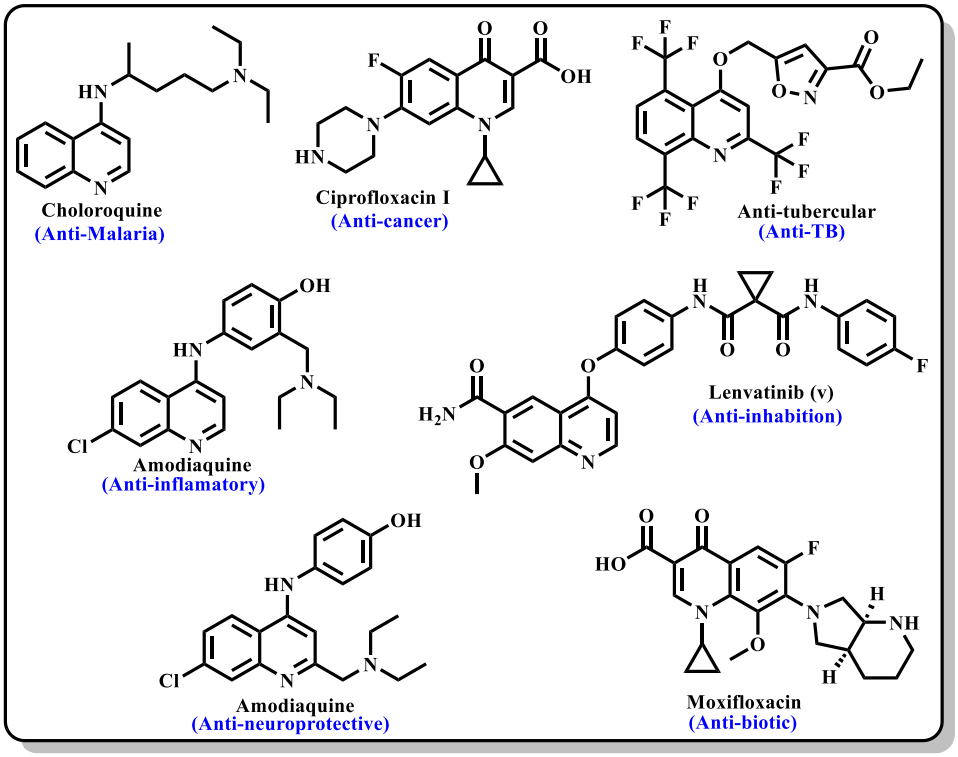

Fig. 1 Various quinoline drugs

2. Result and Discussion

2.1. Chemistry

The synthesis of N-(6,6-dimethyl-8-oxo-9-phenyl-5,6,7,8-tetrahydroacridin-2-yl) aryl sulfonamides (**6a-6j**) and N-(8-oxo-9-phenyl-5,6,7,8-tetrahydroacridin-2-yl) aryl sulfonamides (**10a-10j**) was performed by refluxing (2-amino-5-nitrophenyl)(phenyl) methanone with either 5,5-dimethylcyclohexane-1,3-dione (**2**) or cyclohexane-1,3-dione **(7)** in the presence of a catalytic amount of concentrated hydrochloric acid (0.001 mol) in 10 mL of ethanol for 12 hours. This process yielded either 3,3-dimethyl-7-nitro-9-phenyl-3,4-dihydroacridin-1(2*H*)-one (**3**) or 7-nitro-9-phenyl-3,4-dihydroacridin-1(2*H*)-one (**8**) with a 90% yield. These compounds were subsequently reacted with $SnCl_2$ along with a catalytic amount of con. HCl (0.001 mol) in 10 mL of ethanol. The mixture was then heated to 70 °C for 30 minutes, resulting in the formation of 7-amino-3,3-dimethyl-9-phenyl-3,4-dihydroacridin-1(2*H*)-one (**4**) and 7-amino-9-phenyl-3,4-dihydroacridin-1(2*H*)-one (**9**). Next, these compounds were reacted with various substituted sulfonyl chlorides in the presence of pyridine as a base and 10 mL of dichloromethane (DCM) as the solvent to prepare the final products **6a-6j** and **10a-10j**. The reaction was monitored by TLC to ensure completion, and the crude products were purified by column chromatography. The melting points of the compounds

were measured using a conventional apparatus and reported without correction. Both series of compounds were further characterized using ^{1}H NMR (400 MHz) and ^{13}C NMR (100 MHz), with $CDCl_3$ as the solvent for all NMR analyses. The characteristic peaks in the ^{1}H NMR spectrum appeared for $-CH_3$ and $-CH_2$, as well as aromatic C-H groups, within the ranges of 1-1.2 and 2.5-3.8 δ ppm, respectively. In the ^{13}C NMR spectrum, $-CH_3$ appeared in the range of 26-30 δ ppm, C=O was noted between 190-200 δ ppm, and aromatic C-H was found within 110-165 δ ppm. In the DEPT-135 NMR spectrum, methylene $-CH_2$ groups were identified within the range of 45-56 δ ppm in the negative region. The Fourier transform infrared **(FTIR)** spectrum shows characteristic **N-H**, **C-H**, **C=O**, and **C=C** peaks at **3300-3285** cm^{-1}, **3000-2950** cm^{-1}, **1650-1720** cm^{-1}, and **1540-1570** cm^{-1}, which was further confirmed by high-resolution mass spectrometry **(HRMS)**.

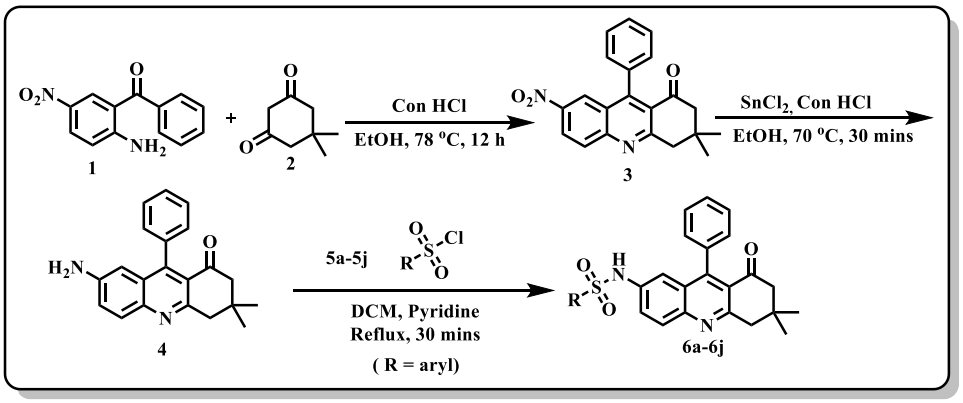

Scheme 1 Synthesis of N-(6,6-dimethyl-8-oxo-9-phenyl-5,6,7,8-tetrahydroacridin-2-yl) arylsulfonamides (**6a-6j**)

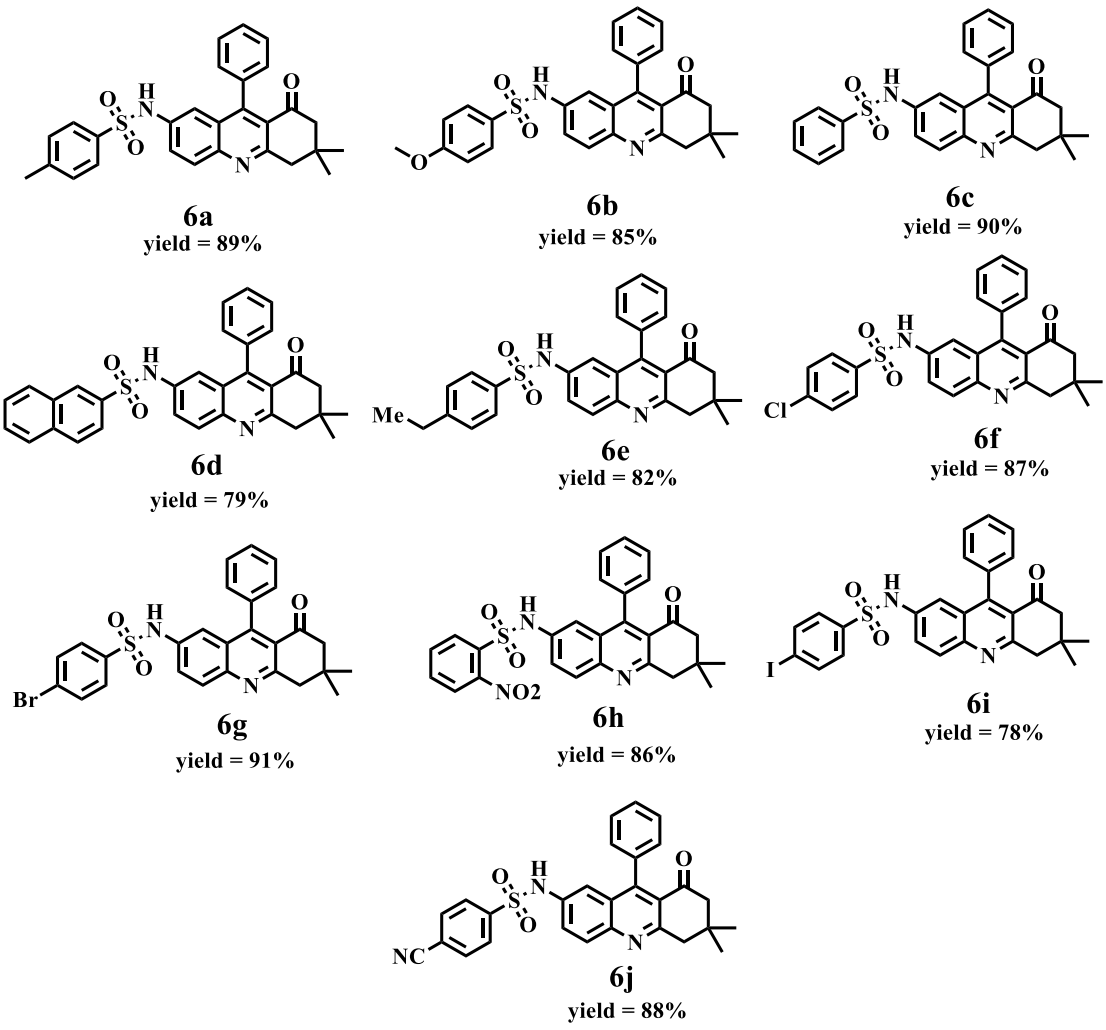

Fig. 2 Substrate Scope **(6a-6j)**

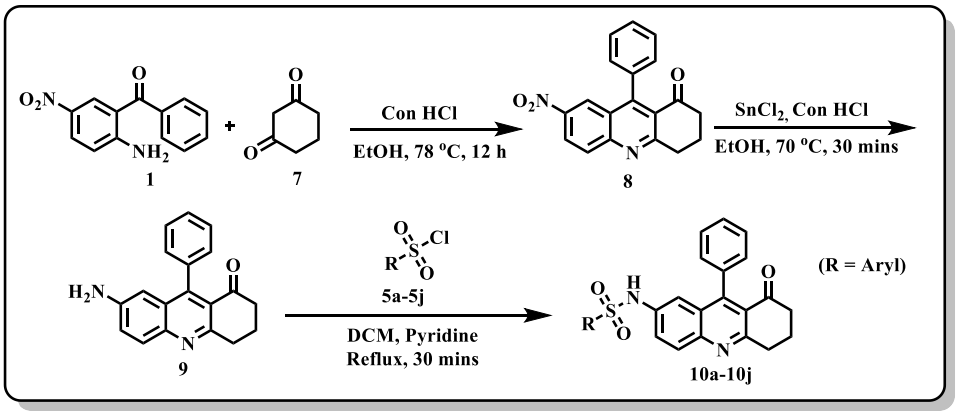

Scheme 2 Synthesis of N-(8-oxo-9-phenyl-5,6,7,8-tetrahydroacridin-2-yl) aryl sulfonamides (**10a-10j**)

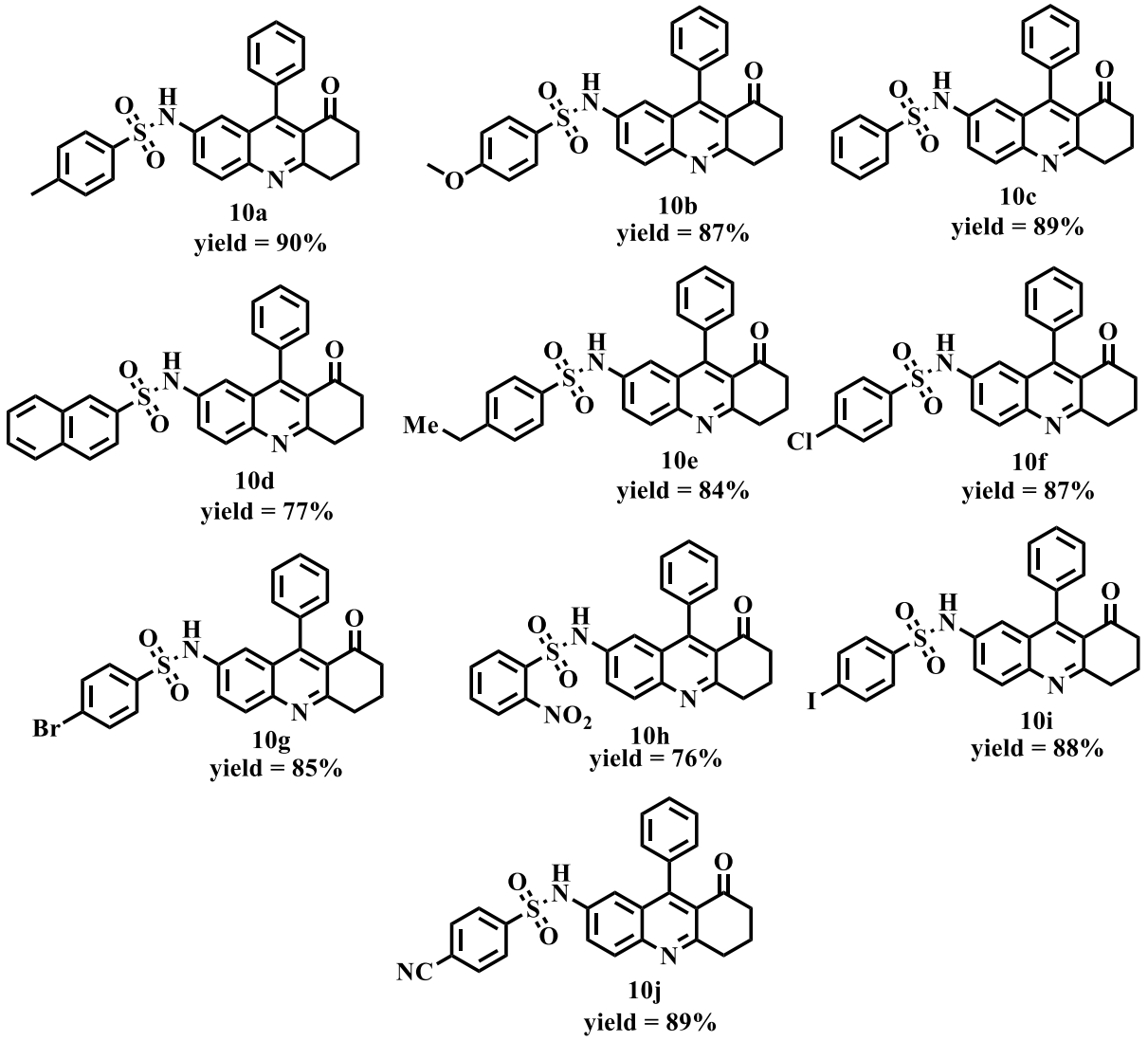

Fig 3 Substrate Scope **(10a-10j)**

2.2. Density Functional Theory

Density Functional Theory was carried out at the B3LYP/6-31+G (d., p) level using Gaussian 09 software. The results were compared among compounds **6a-6j** and **10a-10j**. **Table 1** shows the HOMO and LUMO energy differences ΔE **(eV)**, Ionisation Potential **(IP)**, Electron Affinity **(EA)**, Electronegativity **(χ)**, Chemical Potential **(μ)**, Chemical Hardness **(η)**, Softness **(S)**, and Global Electrophilicity Index **(ω- & ω+)**. Compounds **6b-6d** and **6j** within the **6a-6j** series form a cluster with the largest energy gaps **(~3.65 eV)**, indicating the highest electronic stability and the least reactivity. Similarly, compounds **10a**, **10b**, and **10f** in the **10a-10j** series have the largest energy gaps between HOMO and LUMO, making them the least reactive and most

stable in that series. Among compounds **6a-6j**, **6i** and **6a** are highly reactive due to their small energy difference **(ΔE)**, which allows easier electron transfer and acceptance. Likewise, among compounds **10a-10j**, **10h** and **10e** are reactive because of their small energy gap between two energy levels.

Among the analyses, **6i (4.196 eV)** and **6a (4.365 eV)** from the **6a-6j** and **10e (5.3082 eV)** from **10a-10j** have the lowest ionisation potentials (IPs), indicating a weaker tendency to lose an electron and acting as a donor. This may easily ionise the compound and more reactive towards nucleophiles. Compounds **6h (6.010 eV), 6j (6.115 eV)** from **6a-6j**, and **10f (6.144 eV), 10g (6.031 eV)**, and **10h (6.199 eV)** among **10a-10j** have the lowest negative HOMO energy value, reflecting strongly bound electrons. These compounds have a less electron-donating nature, making them electronically stable and less reactive. The results indicate that electron-withdrawing groups and extended π-conjugation increase HOMO energy, and that IP trends are closely related to molecular stability and reactivity.

Table: 1 DFT calculations of compounds **6a-6j** & **10a-10j**

Cpd. code	HOMO	LUMO	ΔE	IP	EA	χ	μ	η	S	ω	ω-	ω+
6a	-4.365	-3.631	0.734	4.365	3.631	3.998	-3.998	0.367	2.723	21.772	23.817	19.818
6b	-5.948	-2.289	3.658	5.948	2.289	4.118	-4.118	1.829	0.546	4.637	6.925	2.806
6c	-5.964	-2.310	3.653	5.964	2.31	4.137	-4.137	1.826	0.547	4.686	6.983	2.845
6d	-5.926	-2.273	3.653	5.926	2.273	4.099	-4.099	1.826	0.547	4.601	6.879	2.779
6e	-5.305	-2.038	3.267	5.305	2.038	3.672	-3.672	1.633	0.612	4.127	6.167	2.495
6f	-4.796	-2.421	2.374	4.796	2.421	3.608	-3.608	1.187	0.842	5.486	7.438	3.829
6g	-4.646	-3.682	0.963	4.646	3.682	4.164	-4.164	0.481	2.074	17.994	20.13	15.972
6h	-6.01	-2.964	3.045	6.01	2.964	4.487	-4.487	1.522	0.656	6.6117	9.045	4.558
6i	-4.196	-3.488	0.707	4.196	3.488	3.842	-3.842	0.353	2.826	20.861	22.826	18.984
6j	-6.115	-2.481	3.634	6.115	2.481	4.298	-4.298	1.817	0.55	5.083	7.46	3.161
10a	-5.98	-2.316	3.663	5.98	2.316	4.148	-4.148	1.831	0.545	4.697	7.001	2.852
10b	-5.964	-2.311	3.653	5.964	2.311	4.137	-4.137	1.826	0.547	4.686	6.983	2.846
10c	-5.94	-2.295	3.645	5.94	2.295	4.117	-4.117	1.822	0.548	4.651	6.937	2.82
10d	-5.937	-2.292	3.645	5.937	2.292	4.114	-4.114	1.822	0.548	4.645	6.93	2.815
10e	-5.308	-2.041	3.267	5.308	2.041	3.674	-3.674	1.633	0.612	4.133	6.174	2.501
10f	-6.164	-2.405	3.758	6.164	2.405	4.284	-4.284	1.879	0.532	4.885	7.262	2.977
10g	-6.031	-2.394	3.636	6.031	2.394	4.213	-4.213	1.818	0.549	4.881	7.215	3.001
10h	-6.199	-3.361	2.837	6.199	3.361	4.78	-4.78	1.418	0.704	8.052	10.62	5.84
10i	-5.869	-2.23	3.639	5.869	2.23	4.05	-4.05	1.819	0.549	4.506	6.759	2.709
10j	-5.969	-2.500	3.469	5.969	2.5	4.234	-4.234	1.734	0.576	5.169	7.503	3.268

The stability of compounds **6a-6j** and **10a-10j** was further elucidated using FMO calculation parameters and compared with different sulfonamide substituents. Strong electron-withdrawing groups in **10h**, **6j**, **10f**, and **10g (NO$_2$CN, Br, Cl)** lowered the **HOMO** energy, increased the ionisation potential, and decreased electron density on the quinoline ring. This deshielding effect stabilized the molecular orbitals, resulting in a large energy difference between the HOMO and LUMO **(ΔE > 3.60 eV)** and making the derivatives more electronically stable. Moderately electron-withdrawing groups, such as **Cl**, **Br**, and aromatic substituents **(6b, 6c, 6d, 10a-10d, 10g),** also improve stability by lowering HOMO energy values and increasing chemical hardness, resulting in high kinetic and thermodynamic stability.

In contrast, molecules with electron-donating groups **(EDGs)**, such as methyl **(6a)**, and heavily substituted alkyl groups **(6e, 10e)** destabilised the FMO distribution by increasing HOMO energies and reducing **ΔE** values. This enhances the softness and reactivity of these derivatives. Compounds **6g** and **6i** contain extended conjugated substituents, which make the compounds more polarizable, which is the reason for **low ΔE (<1.0 eV)**, indicating high reactivity due to increased HOMO delocalisation and more feasible electron transfer. Derivatives with moderately donating and weakly withdrawing groups **(6e, 10e, 10i, 10j, 6h)** show **intermediate ΔE** values, indicating medium stability due to partial stabilisation of π-system. Overall, the trend clearly shows that strong electron-withdrawing groups stabilise the FMO energies, increase hardness, and widen the HOMO-LUMO energy gap. Electron-withdrawing groups destabilise the orbitals, reduce ΔE, and heighten reactivity. Hence, substituent electronic effects are crucial, with **10h**, **10f**, **10j,** which were shown in **Figure 5**, and **6h**, **6f**, **6j** emerging as the most stable and chemically inert. The HOMO and LUMO energy difference diagrams of compounds **6f**, **6h**, and **6j** are shown in **Figure 4**.

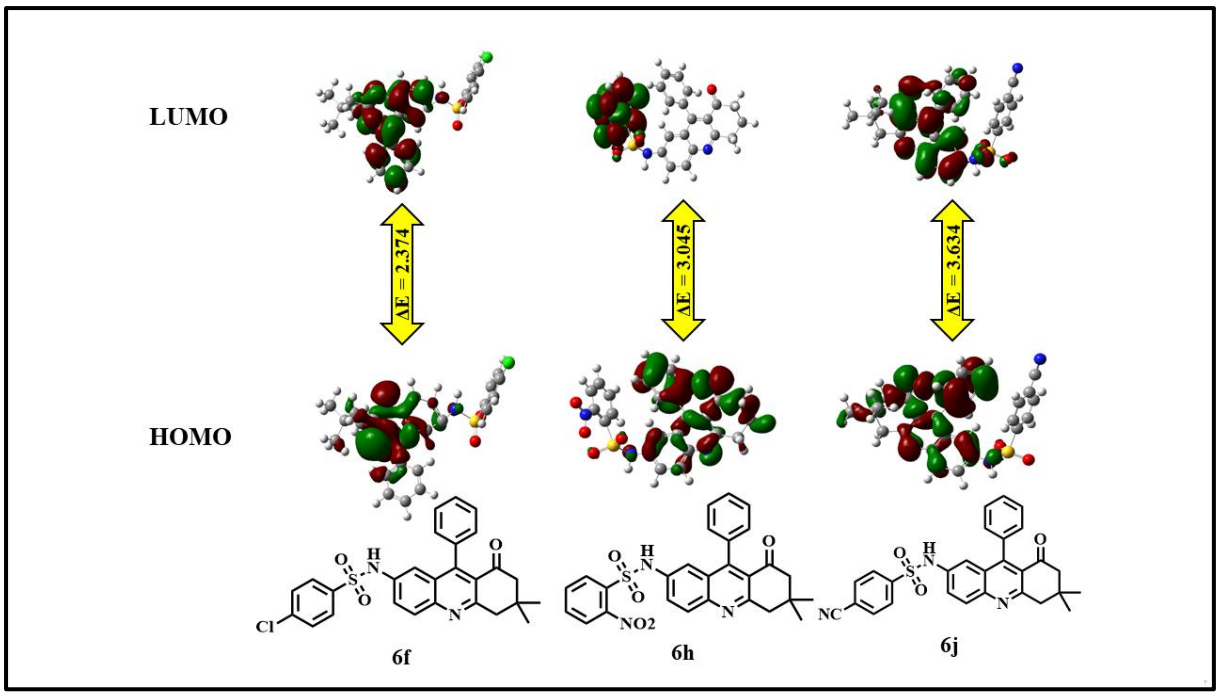

Fig. 4 HOMO-LUMO energy gap of compounds **6f**, **6h**, and **6j**

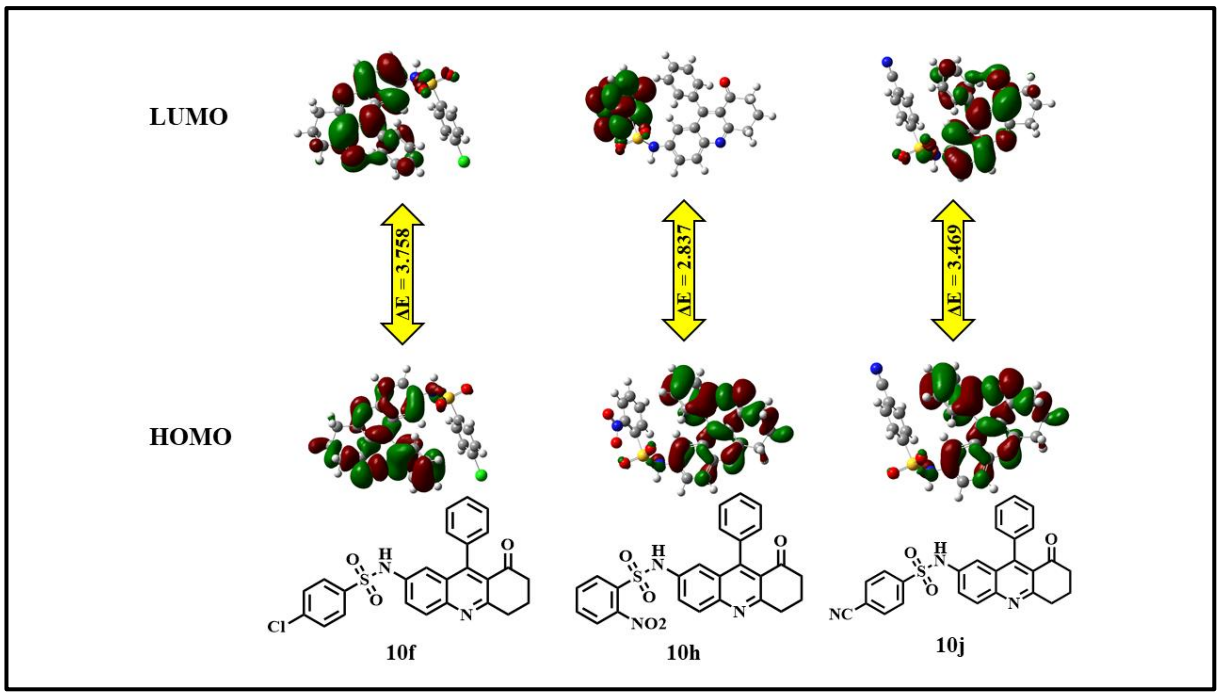

Fig. 5 HOMO-LUMO energy gap of compounds **10f**, **10h**, and **10j**

2.3. Molecular Electrostatic Potential

MEP analysis shows that in **6a-6j**, compounds **6f**, **6h** and **6j**, and in **10a-10j**, compounds **10f**, **10h**, and **10j** have the most electron-rich regions **(deep red colour**), which are delocalized around the carbonyl oxygen, sulfonyl oxygen, and heteroatoms, and also have a strong **H-Bond** accepting ability. The **N-H** atom is responsible for the electron-poor region **(blue colour)**. In **6f**, **6h**, and **6j**, the

carbonyl oxygen and sulfonyl oxygen act as donating nucleophiles, and the **N-H** acts as an H-bond donor during receptor binding. Similarly, **10f** shows the most intense negative potential near the carbonyl oxygen, which acts as a strong nucleophile and interacts more strongly with the positively charged residue within the active site present in the protein. Compound **10h** shows a distributed negative potential around the carbonyl and aromatic substitution in the **4th** position, and the blue region around the halogen atom is due to electrophilic behaviour, which favours halogen-bond interaction. Compound **10j** has a distributed electrostatic potential and a moderate negative region around heteroatoms and a positive region around the substituted aromatic ring. Overall, the ligands from **6a-6j** and **10a-10j** show distinctive electrostatic characteristics that directly influence their docking affinities and binding behaviour. In **Figure 6**, the most notable interaction patterns are governed by the molecular electrostatic potential **(MEP)**. The other derivatives follow similar trends and are documented separately in the supplementary materials for completeness.

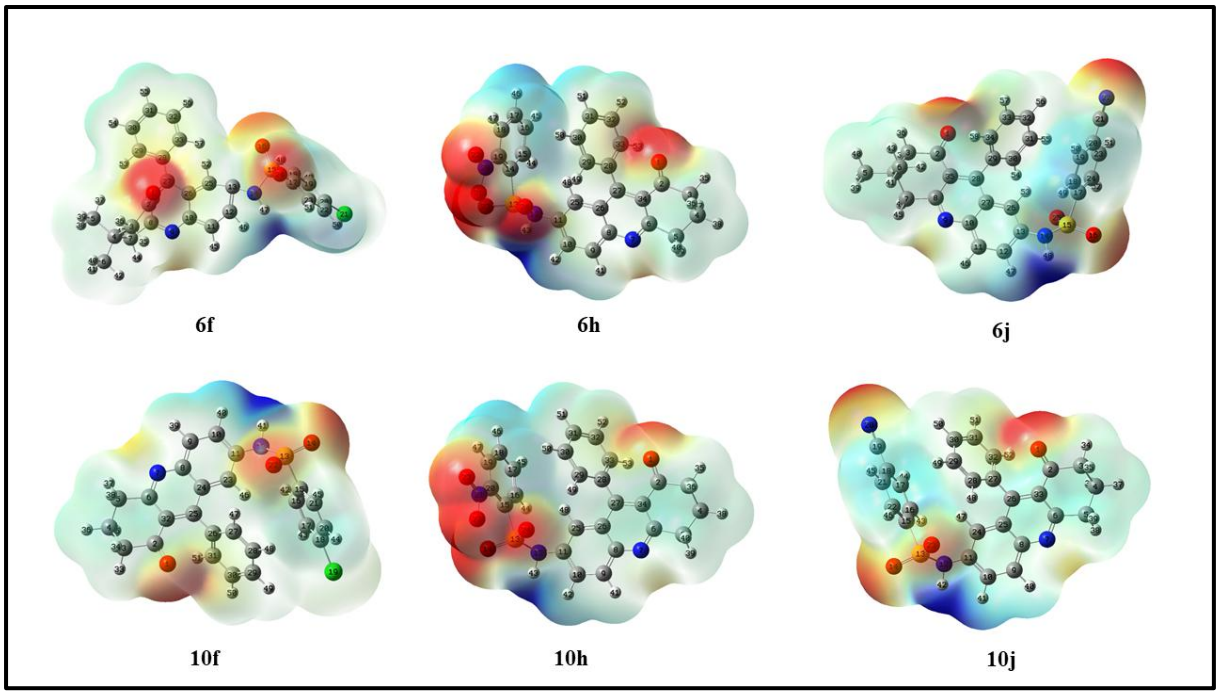

Fig. 6 MEP diagram for compounds **6f**, **6h**, **6j**, **10f**, **10h**, and **10j**

2.4. Docking Studies

Molecular docking is the key computational method used to predict the interaction with a target protein, helping to understand binding modes and support drug design studies. In this work, docking was performed to analyse the interaction patterns of selected ligands with the target protein. The protein pdb **(9cm2)** was downloaded from the Protein Data Bank (PDB). AutoDock Vina is used to perform molecular docking, and the resulting ligand-protein

complexes were visualised and analysed in **Discovery Studio**, allowing identification of key residues and significant non-covalent interactions.

Molecular docking studies were performed to study the binding nature with the residue of the synthesised quinoline derivatives **6a-6j** with the target protein, using cidofovir as the reference standard. Among these, ligand **6d** shows the highest binding affinity of **(-11.1 kcal/mol)** with an **RMSD** of **4.50 Å** and the lowest **Ki (0.0071 µM)**, indicating highly stable and favourable for binding at the active site of the protein. In **Figure 7**, **2D** interaction diagram reveals the presence of a conventional **H-bond** with **THR414** (3.02 Å), a **π-sulfur** interaction with **TRA480** (4.36 Å), and a dual **π-π stacking** interaction with **PHE483** (3.82 & 4.18 Å), and also with multiple van der Waals interactions **(GLU415, ASN476, GLY413, HIS412, LEU479,** and **ARD550)**, that contribute to complete pocket filling.

Ligand **6h** has a strong binding affinity of **-10.8 kcal/mol**, with an **RMSD** of **2.91 Å**, and a low **Ki** value **(0.011 µM)**. **2D** interaction image shows a **π-π T-shaped** interaction with **PHE483** (5.40 Å), which orients the aromatic ring within the binding pocket and provides key stabilisation. Van der Waals interactions with **ASP405, GLU410, HIS412, ILE09, GLY413, THR414, ASN476, LEU479**, and **TRP480** extensively stabilize it.

Table 2 Docking scores with Adenovirus **(PDB: 9cm2)**

Ligand	Binding Affinity (kcal/mol)	RMSD (Å)	Ki (µM)	Ligand	Binding Affinity (kcal/mol)	RMSD (Å)	Ki (µM)
6a	-10.3	1.80	0.0278	**10a**	-9.8	1.39	0.0647
6b	-10.4	2.61	0.0235	**10b**	-10.0	1.25	0.0461
6c	-10.1	1.19	0.0389	**10c**	-9.6	1.33	0.0906
6d	**-11.1**	4.50	0.0071	**10d**	**-10.8**	1.69	0.0119
6e	-10.7	1.78	0.0141	**10e**	-10.0	1.52	0.0461
6f	-10.2	1.83	0.0329	**10f**	-10.1	3.04	0.0389
6g	-9.3	2.09	0.150	**10g**	-9.2	1.66	0.150
6h	**-10.8**	2.91	0.0119	**10h**	-9.5	2.19	0.107
6i	-10.2	1.80	0.0329	**10i**	-10.2	1.03	0.0329
6j	-10.1	2.76	0.0389	**10j**	-10.3	0.91	0.0278

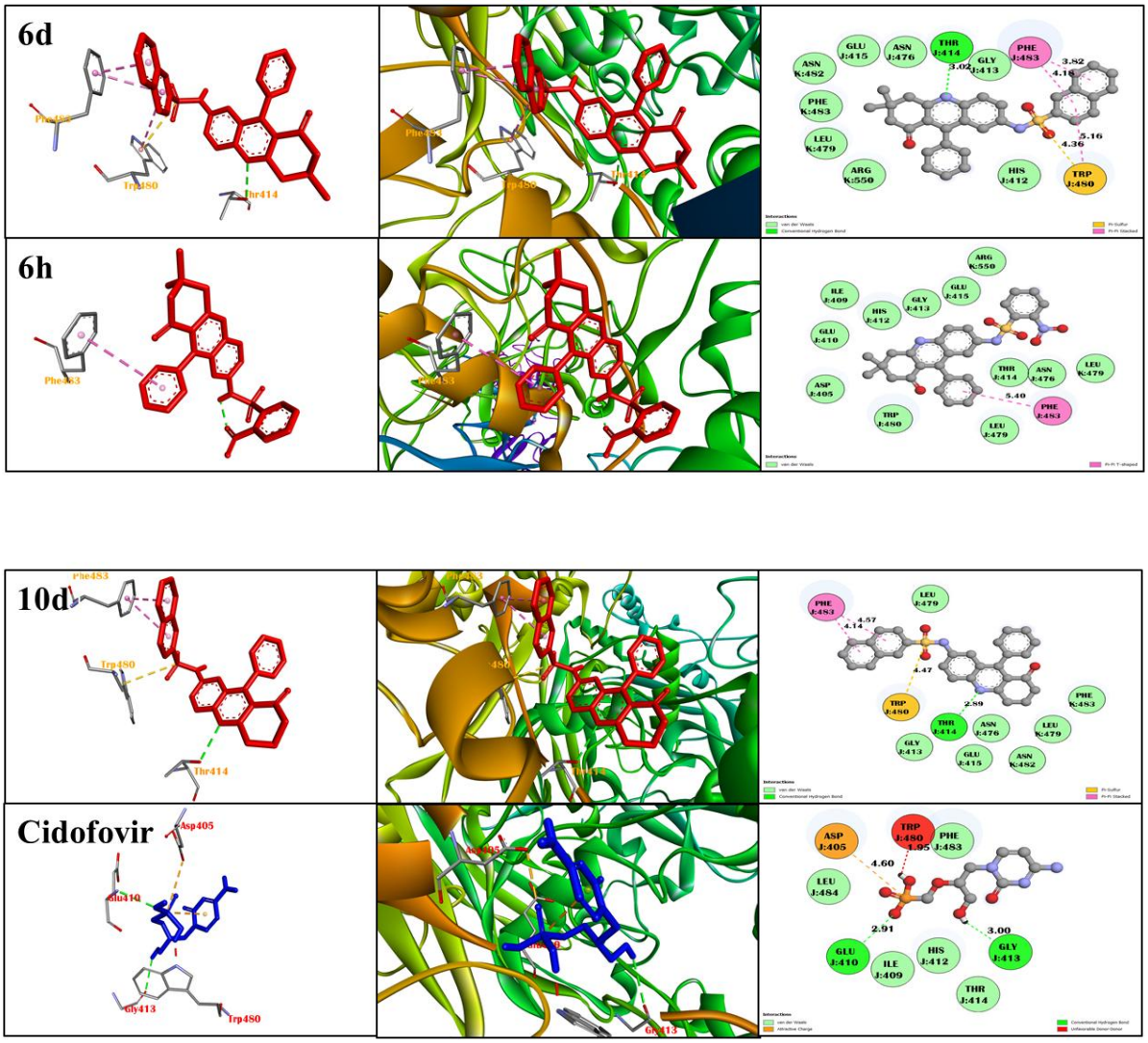

Fig 7 2D and 3D image of compounds **6d**, **6h**, and **10d** with pdb **(9cm2)**

In compounds **10a-10j**, ligand **10d** has the highest docking score of **-10.8 kcal/mol** and a low **Ki (0.0119 µM).** This ligand forms an effective **H-Bonding** with **THR414** (2.89 Å), **π-π stacking** interaction with **PHE483** (4.14 & 4.57 Å), and a **π-sulfur** interaction with **TRA480** (4.47 Å), further strengthening the nature of hydrophobic anchoring, indicating that the **10d** effectively engages in multi-faceted non-polar contacts. Surrounding van der Waals interactions with critical residues such as **ASN476**, **LEU479**, **GLU415**, **ASN482**, and **GLY413** enhance hydrophobic binding. Ligands **6d**, **6h**, and **10d** show overall better binding affinity compared to the standard drug Cidofovir used, due to richer **H-Bonding**, **π-π stacking**, and **hydrophobic** interactions. Their superior Docking scores and stability show effectiveness against antivirals.

2.5. Absorbance and emission studies

The photophysical properties of the compounds **6a-6j** and **10a-10j** were measured over approximately **473-263** nm. In these two series, structural rearrangement influences the excited-state behaviour of the compounds. The dimethyl substituent in **6a-6j** acridinone core acts as a chromophore and is fused to the acridine ring, whereas compounds **10a-10j** are comparatively less sterically hindered and planar. These small structural changes affect the electron distribution on the intramolecular π-system. Introducing a dimethyl group into the acridinone creates torsional strain between the acridinone core and the aryl sulfonamide ring, restricting conjugation and increasing the vibrational degrees of freedom. The non-radiative relaxation processes were not involved in the emission of radiation, reflected in the low quantum yield of compound **6c** at **0.001**. In compounds **10a-10j**, a planar geometry of acridinone extends the delocalisation of π-electrons toward the phenyl ring that is covalently attached to the sulphonamide substitution, enhancing non-radiative decay and radiative deactivation with the quantum yield of **0.187**.

The electron-donating **(-OCH_3 & CH_3)** groups in compounds **6a-6j** and **10a-10j** promote intramolecular charge transfer **(ICT)** and π-extended electron conjugation from the donor ring to the carbonyl acridinone, stabilising the excited state energy and resulting in red-shifted absorption and emission spectra. In **10a-10j**, at **422 nm**, the wavelength indicates enhanced intramolecular charge transfer due to the planar geometry. Halogen-substituted compounds **(6g, 6i, 6f, 10g, 10i, and 10g)** increase intersystem crossing **(ISC)** towards the triplet state, which can quench fluorescence. Strong electron-withdrawing groups on **6h** and **10h (NO_2 & CN)** create strong intersystem crossing towards triplet states that are often non-radiative, acting as a chromophore, and leading to high quantum yields of **0.103** and **0.171**. Similarly, **6j** and **10j** also produce higher yields of **0.088** and **0.113**.

Table 3 Photophysical calculation for compounds **6a-6j** & **10a-10j**

S I	$\lambda_{Absorption}$	$\lambda_{Emission}$	Stoke Shift Δ × 10^4	Molar Extinction Coefficient × 10^4	Quantum Yield (ϕ)
6a	247.8	421.4	2.061	1.05	0.099
6b	262.2	422	1.79	1.46	0.099
6c	253.2	421.5	1.955	137	0.001
6d	261.3	421.5	1.803	1.54	0.085
6e	261.2	421.5	1.805	1.38	0.112
6f	256.1	420	1.889	1.4	0.066

6g	260.6	421	1.812	1.38	0.101
6h	259.4	422.5	1.845	1.28	0.103
6i	250.1	421.5	2.016	1.46	0.048
6j	246.9	422.5	2.087	1.01	0.088
10a	260.8	423.5	1.826	1.06	0.161
10b	261.4	435	1.893	1.32	0.105
10c	262.2	446.5	1.952	0.94	0.109
10d	262.4	422.5	1.79	1.24	0.122
10e	261.8	435	1.885	1.1	0.126
10f	260.5	425	1.842	1.29	0.1
10g	261.4	429	1.853	0.82	0.187
10h	261.9	421.5	1.792	0.83	0.171
10i	249.5	424.5	2.048	0.86	0.094
10j	263	422	1.776	1.14	0.113

The Stokes shift calculations indicate larger shifts for compounds **6a**, **6j**, and **10i** due to higher excited-state energies. The molar extinction coefficients for compounds **6a** through **6j** were comparable to those of compounds **10a** through **10j**, suggesting that aromatic para-ring substitutions have minimal impact on the ground-state oscillator strength. However, the high molar extinction coefficient for **6c** is an exception and does not significantly influence the overall trends. A key difference between the two sets of compounds (**6a-6j** and **10a-10j**) is their fluorescence quantum yields. The compounds **10a-10j** exhibit higher emission efficiencies compared to **6a-6j**. For compounds with equivalent substituents, the presence of cyano (CN), nitro (NO_2), and bromo (Br) groups at the 4th position notably enhances the quantum yield, particularly in **10g** and **10h**, which achieve maximum efficiency. While compound **6c** was nearly non-emissive, its counterpart **10c** showed moderate fluorescence, highlighting the significant role of the core structure in the decay pathways.

Overall, these photophysical studies indicate that the structural design of compounds **10a-10j** improves the stability in the excited state and reduces non-radiative decay, resulting in higher quantum yields and **red-shifted** emissions for specific substituents. The enhanced photophysical properties of compounds **10a-10j** suggest a more favourable electronic environment for fluorescence, likely attributable to improved conjugation, increased rigidity, or reduced intersystem crossing. These characteristics position the **10**-series as the preferred chromophore platform for the development of advanced emissive functional materials.

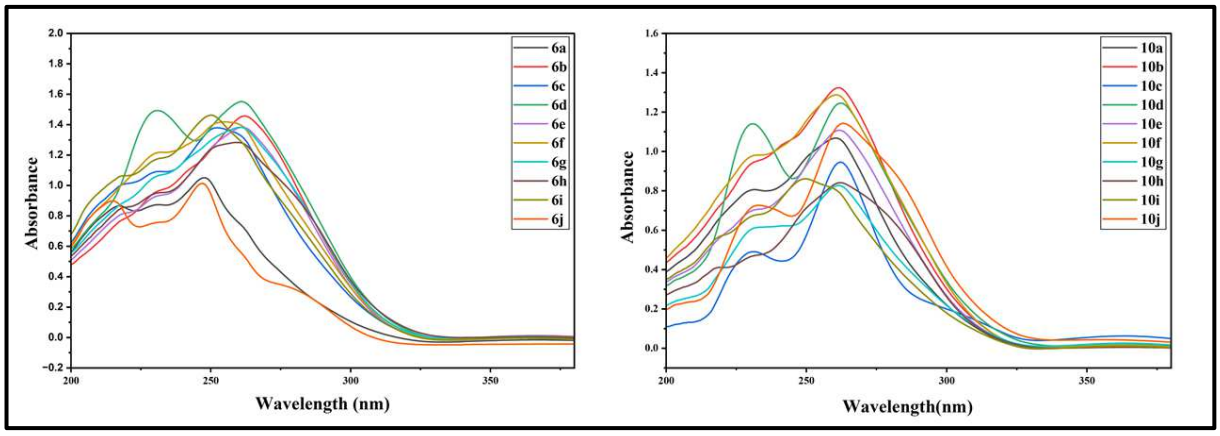

Fig. 8 UV-visible spectra of compounds **6a-6j** and **10a-10j** in ethanol solution

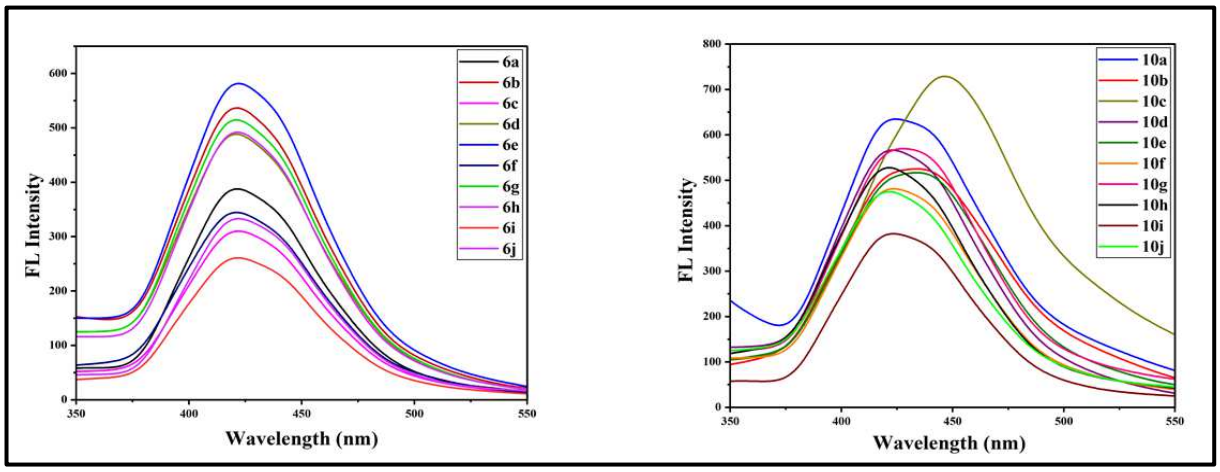

Fig. 9 Fluorescence spectra of compounds **6a-6j** and **10a-10j** in ethanol solution

3. Experimental procedure

3.1. General procedure for preparation of 6a-6j & 10a-10j

A mixture containing 7-amino-3,3-dimethyl-9-phenyl-3,4-dihydroacridin-1(2*H*)-one **(0.001 mmol, 1.0 equiv.)**, substituted sulfonyl chloride **(0.0015 mmol, 1.5 equiv.)**, and pyridine base **(0.003 mmol, 3.0 equiv.)** in DCM solvent. The reaction was refluxed for 30 min in a round-bottom flask. TLC is used to monitor the reaction. Then, the crude mixture was added to ice-cold water, and the **pH** was adjusted to **7-8** with **10% HCl**. The product was extracted with ethyl acetate **(2 x 100 mL)**. The organic solvent was washed with a 40% brine solution, filtered over **Na_2SO_4** to remove moisture. The solvent was evaporated by steam distillation. The crude mixture was purified by column chromatography **(60-120 mesh)** using ethyl acetate/hexane as the eluent, yielding the pure compounds of **6a-6j** and **10a-10j**.

Quantum yield calculation

$$\phi_f = \phi_R \cdot A_R/A \cdot I/I_R \cdot n^2/n^2_R \textbf{ (1)}$$

$\boldsymbol{\phi_f}$ = Quantum yield, **I** = Integrated fluorescence emission

A = Absorbance at excitation wavelength, **n** = Refractive index of solvent

R = Quinine sulphate, $\boldsymbol{\phi_R}$ = Quantum yield of reference

Stoke' s shift was determined using the following equation:

$$\Delta \bar{\nu} = 10^7 / \lambda_{\text{max (absorption)}} - 10^7 / \lambda_{\text{max (emission)}} \textbf{ (2)}$$

4. Conclusion:

In this study, **6a-6j** and **10a-10j** were characterized using **NMR**, **FTIR**, **HRMS**, and photophysical techniques. Density Functional Theory **(DFT)** calculations show that the electronic properties of different substituted sulfonyl chlorides differ, based on the nature of the substituent. Electron-withdrawing groups **(EWGs)** increase the stability by expanding the **HOMO-LUMO** energy difference **(ΔE)**, while electron-donating groups **(EDGs)** enhance softness and reactivity. Molecular Electrostatic Potential **(MEP)** analyses mapped the key regions responsible for molecular recognition. Docking studies show that **6d**, **6h**, and **10d** compounds have higher binding affinity than cidofovir, due to stronger interactions and better binding pockets, as evidenced by **lower Ki** values. It suggests that compounds **6d**, **6h**, and **10d** exhibit antiviral activity. Photophysical experiments demonstrated that the 10-series had improved fluorescence, likely due to increased planarity and stabilization of the excited state. Overall, the data support acridinone-sulfonamide hybrids as promising bioactive and photoactive compounds, with **6d**, **6h**, and **10d** identified as key leads for future antiviral development.

Acknowledgement

The authors would like to express their sincere gratitude to the Vellore Institute of Technology in Vellore for providing the infrastructural support and characterization facilities that facilitated.

Funding Declaration

This work has been supported by the Vellore Institute of Technology through the seed grant SG20230086.

Conflicts of interest

There are no conflicts of interest.

Supportive Information

All spectroscopic data, including ^{1}H, ^{13}C NMR, DEPT-135 and two-dimensional NMR of various compounds, and high-resolution mass spectrometry (HRMS) data, as well as frontier molecular orbital (FMO) diagrams for the respective molecules, are available in PDF format.

Data Availability Statement

The data is included in the manuscript, along with the supplementary information file.

CRediT authorship contribution statement:

Shanmugavel Balamurugan: Writing-Original draft, Data Curation, and Formal Analysis. **Vijayaparthasarathi Vijayakumar:** Writing-Review & Editing, Funding Acquisition, Validation, Methodology, and Conceptualization.

Reference

[1] O. S. Travkina, A. S. Artem'eva, A. K. Ishkildina, I. N. Pavlova, D. V. Serebrennikov, N. G. Grigor'eva, B. I. Kutepov, *Pet. Chem*, 2024, (64). 245–257. https://doi.org/10.1134/S0965544124030022

[2] J. R. Li, L. J. Zhang, X. Q. Yang, Q. Li, D. Wang, C. X. Wang, D. X. Shi, Q. Zhang, *Chin. Chem. Lett,* 2008, (19), 15–18. https://doi.org/10.1016/j.cclet.2007.11.003.

[3] Q. W. Pan, J. H. Wang, Q. Wang, H. J. Li, Y. C. Wu, *ChemistrySelect*, 2020, (5), 4099–4103. https://doi.org/10.1002/slct.202000895.

[4] J. C. Sloop, *J Phys Org Chem*, 2009, (22), 110–117. https://doi.org/10.1002/poc.1433.

[5] D. Zheng, R. Huang, H. Lan, *Results Chem*, 2025, (16), 102523. https://doi.org/10.1016/j.rechem.2025.102523.

[6] M. Tour, S. Cojean, *Eur. J. Med. Chem*, 2025, (13), 100241.

[7] C. Gao, R. Li, Y. Li, Y. Wu, Y. Qu, M. Ampomah-Wireko, J. Zheng, Z. Wang, Y.N. Wang, E. Zhang, *Bioorg Chem*, 2025, (162). https://doi.org/10.1016/j.bioorg.2025.108579.

[8] V. Solanki, M. Ibrahim, A. Doshi, A. K. Das, H. Sarvaiya, V. Jain, Y. Jadeja, Chem Biodivers (2025). https://doi.org/10.1002/cbdv.202500646.

[9] A. Aldhahrani, N. A. Alshaye, D. S. Alshaya, D. A. Mohamed, E. Fayad, M. A. E. Sophy, N. A. Al-Ashger, M. G. Salem, N. A. Farouk, *J Mol Struct*, 2025, (1326), 141060. https://doi.org/10.1016/j.molstruc.2024.141060.

[10] N. J. Pravin, R. S. Kavalapure, S. Gharge, S. G. Alegaon, S. D. Ranade, L. S. Wong, R. Ramu, *ACS Omega*, 2025, (10), 33712–33730. https://doi.org/10.1021/acsomega.5c04663.

[11] V. K. Singh, S. Rai, A. S. Parihar, I. Ahmad, H. Patel, D. Schols, R. K. Singh, *J Mol Struct*, 2025, (1319), 139531. https://doi.org/10.1016/j.molstruc.2024.139531.

[12] J. P. Suchitra, J. C. Rhoda, V. Bharathi Devi, P. Divya, H. M. Albert, *J Fluoresc*, 2025, (35), 2785–2794. https://doi.org/10.1007/s10895-024-03724-7.

[13] D. Kumar, P. Verma, M. Chaudhary, S. Ali, A. Singh, *J Mol Struct*, 2025, (1319), 139515. https://doi.org/10.1016/j.molstruc.2024.139515.

[14] F. Imanifard, M. Daghighi Asli, E. Najafi, B. Notash, *Iran. J. Chem. Chem. Eng*, 2025, (44), 150–161. https://doi.org/10.30492/ijcce.2024.2030552.6635.

[15] A. Srivastava, S. Shukla, A. Meshram, *Sustain. Metall*, (2025). https://doi.org/10.1007/s40831-025-01243-8.

[16] B. Mustapha, A. A. Saleh, R. El-Seifat, S. Bufarwa, H. Hasan, D. Moustafa, *Appl Organomet Chem*, 2025, (39), 1–23. https://doi.org/10.1002/aoc.70310.

[17] Y. Senpradit, S. Wacharasindhu, M. Sukwattanasinitt, Spectrochim Acta A Mol Biomol Spectrosc, 2025, (326), 125128. https://doi.org/10.1016/j.saa.2024.125128.

[18] J. E. Nycz, J. Kolińska, N. Karaush-Karmazin, T. Chen, M. Książek, J. Kusz, *Molecules*, 2025, (30), 1–28. https://doi.org/10.3390/molecules30122659.

[19] M. A. Vora, H. M. Parekh, *Talanta*, 2026, (299), 129067. https://doi.org/10.1016/j.talanta.2025.129067.

[20] J. C. Sloop, *J Phys Org Chem*, 2009, (22), 110–117. https://doi.org/10.1002/poc.1433.

[21] A. Bouzina, C. Benzaid, H. Bentoumi, Y. O. Bouone, M. L. Djendi, R. Mansouri, R. Sayad, N.E. Aouf, *J Mol Struct*, 2025, (1347), 143317. https://doi.org/10.1016/j.molstruc.2025.143317.

[22] S. Jalil, Z. Hussain, S. M. A. Abid, A. Hameed, J. Iqbal, *RSC Adv*, 2024, (14), 8905–8920. https://doi.org/10.1039/d3ra05501a.

[23] K. Xue, Z. Xu, P. Sun, Y. He, Z. Zhou, X. Huang, L. Liu, *Med. Chem. Res*, 2025, 2547–2557. https://doi.org/10.1007/s00044-025-03475-5.

[24] N. N. Soliman, A. A. Fadda, H. E. Gaffer, N. M. Bayoumy, *Sci Rep*, 2025, (15), 1–16. https://doi.org/10.1038/s41598-025-16561-w.

[25] W. R. Swift-Ramirez, G. A. Weiss, *European J Org Chem*, 2025, 2500400. https://doi.org/10.1002/ejoc.202500400.

[26] M. Zala, J. J. Vora, V. M. Khedkar, A. H. Almalki, S. Tivari, R. Jatvada, *ACS Omega,* 2025, (10), 7120–7130. https://doi.org/10.1021/acsomega.4c10198.

[27] C. M. Al-Matarneh, N. Simionescu, A. Nicolescu, M. Silion, A. Angeli, N. Paoletti, A. Bonardi, P. Gratteri, M. Pinteala, C. T. Supuran, *J Med Chem*, 2025, (68), 1863–1882. https://doi.org/10.1021/acs.jmedchem.4c02586.

[28] O. A. A. Ali, A. Ragab, Y. A. Ammar, M. S. Abusaif, *J Mol Struct*, 2025, (1334), 141879. https://doi.org/10.1016/j.molstruc.2025.141879.

[29] Z. Saifi, A. Ali, A. Inam, A. Azam, M. Kamthan, M. Abid, I. Ali, *RSC Adv*, 2025, (15), 1680–1689. https://doi.org/10.1039/d4ra05069j.

[30] P. Panduranga, P. Makam, N. Kumar Katari, R. Gundla, S. Babu Jonnalagadda, B. Kumar Tripuramallu, *ChemistryOpen*, 2025, (14), 1–9. https://doi.org/10.1002/open.202400334.

[31] M. Gensicka-Kowalewska, G. Cholewiński, K. Dzierzbicka, *RSC Adv*, 2017, (7), 15776–15804. https://doi.org/10.1039/c7ra01026e.

[32] M. Shaldam, A. Nocentini, Z. M. Elsayed, T. M. Ibrahim, R. Salem, R. A. El-Domany, C. Capasso, C.T. Supuran, W.M. Eldehna, *Int J Mol Sci*, 2021, (22). https://doi.org/10.3390/ijms222011119.

[33] N. D. Chavan, S. Sarveswari, V. Vijayakumar, *Sci Rep*, 2025, (15), 1–18. https://doi.org/10.1038/s41598-025-94817-1.

[34] S. A. Aloudah, A. A. Fadda, E. Abdel-Latif, E. Nabil, M. Zakaria, *J Mol Struct*, 2026, (1350), 144024. https://doi.org/10.1016/j.molstruc.2025.144024.

[35] H. E. Gaffer, S. A. Mahmoud, M. S. El-Sedik, T. Aysha, M. H. Abdel-Rhman, E. Abdel-latif, *Sci Rep*, 2024, (14), 1–17. https://doi.org/10.1038/s41598-024-60908-8.

[36] H. G. El-kasabi, M. M. Girges, S. A. A. El-Salam, A. E. Suliman, G. E. Abdel-Ghani, *Sci Rep*, 2025, (15), 1–18. https://doi.org/10.1038/s41598-025-06248-7.

[37] P. Panduranga, P. Makam, N. Kumar Katari, R. Gundla, S. Babu Jonnalagadda, B. Kumar Tripuramallu, *ChemistryOpen*, 2025, (14), 1–9. https://doi.org/10.1002/open.202400334.

[38] J. Iqbal, T. Islam, M. al-Rashida, A. Hameed, T. Iftikhar, J. Pelletier, J. Sevigny, S. Alrokayan, M. Maqbool, K. Ayub, T. Hussain, *Results Chem*, (17). https://doi.org/10.1016/j.rechem.2025.102556.

[39] J. Sun, J. Chen, Y. Lou, Z. Chen, X. Jiang, J. P. Monserrat, Y. Zhang, L. Shen, *Eur J Med Chem*, 2026, (301), 118170. https://doi.org/10.1016/j.ejmech.2025.118170.

[40] M. S. Elkotamy, M. K. Elgohary, I.A. Elkelesh, M. A. Alkabbani, E. F. Khaleel, W. M. Eldehna, H. A. Abdel-Aziz, *Bioorg Chem*, 2025, (157), 108247. https://doi.org/10.1016/j.bioorg.2025.108247.

[41] Y. Jia, S. Bahraminejad, X. Duan, S. Kong, A. Taledaohan, C. Jiang, D. Ma, J. Jiang, Y. Wang, J. Liu, *Eur J Med Chem*, 2025, (296), 117830. https://doi.org/10.1016/j.ejmech.2025.117830.

[42] S. Das, P. Sunnapu, M. Rafi, Y. Begum, S. Dey, A. Joshi, N. Singh, K. G. Thakur, P. Jaisankar, U.P. Singh, *Mol Divers*, 2025. https://doi.org/10.1007/s11030-025-11315-2.

[43] P. Yadav, A. A. Varma, P. Gopinath, Chem. Commun, 2025, (1), 16440–16443. https://doi.org/10.1039/d5cc04023j.

[44] A. Zieba, D. Pindjakova, M. Latocha, J. Plonka-Czerw, D. Kusmierz, A. Cizek, J. Jampilek, *Molecules*, 2024, (29), 1–22. https://doi.org/10.3390/molecules29174044.

[45] C. M. Eteghwia, E. Ojaikre, E. A. Onoabedje, C. C. Eze, P. O. Adomi, Phys. Commun, 2025, (12), 141–149. https://doi.org/10.4314/cps.v12i1.11.

[46] G. Sandya Rani, S. Sravani, C. Bhavani, A. Nagaraju, P. Asmathunisa, A. Shashi, V. Rao, M. Shivashankar,, *Synthesis 3*, 2024, 609–613. www.allmultidisciplinaryjournal.com.

Supplementary Files

This is a list of supplementary files associated with this preprint. Click to download.

- SupportiveInformation.docx